A COMPLETE AERODYNAMIC ROUGHNESS MAP DERIVED FROM ROCK ABUNDANCE DATA: EXTRAPOLATION TO HIGH LATITUDES

C. Listowski , *Laboratoire ATmosphères, Milieux, Observations Spatiales (LATMOS), Université Versailles St Quentin (UVSQ), Guyancourt, France, (constantino.listowski@latmos.ipsl.fr),* **E. Hébrard**, *Université de Bordeaux, Laboratoire d'Astrophysique de Bordeaux, CNRS/INSU, UMR 5804, BP 89, Floirac Cedex, F-33271, FRANCE.,* **A. Määttänen**, *LATMOS, UVSQ, Guyancourt, France,* **F. Montmessin**, *LATMOS, UVSQ, Guyancourt, France.* **F. Forget**, *LMD, CNRS/INSU-IPSL-Université Paris 6 Pierre et Marie Curie, Paris, F-75252, FRANCE.*

Introduction: Dust storms have been reported in all seasons on Mars from ground-based and spacecraft observations, across much of the planet and ranging from small local storms covering a few tens of km^2 to planet encircling [1]. Simulations of these dust events using Mars Global Circulation Model (MGCM) indicates that the large quantities of dust lifted into the atmosphere during these storms can have a strong impact on the atmospheric thermal structure, the global circulation patterns and thus the climate in general [2]. Further understanding of the origin of these local and global dust storms strongly implies the description of the processes involved in dust rising and transportation from the Martian surface. Looking at observations, it is almost certain that aeolian erosion varies from one region to another depending on the ease of dust lifting from the surface [3]. Yet, until recently, there have not been enough data available in modern MGCMs to implement a spatially variable wind stress threshold map nor, for that matter, any map for the factors that are controlling (interparticle cohesion, surface roughness, etc). The aerodynamic roughness length z_0 especially affect the model-calculated wind stresses and wind stress thresholds for dust lifting; a spatially varying aerodynamic roughness length field could thus affect the simulated dust cycle [4].

Parametrization of the aerodynamic roughness height z_0: The spatial variations of the aerodynamic roughness length z_0 has not been fully investigated yet on Mars, and latest MGCM simulations have assumed a spatially uniform aerodynamic roughness length z_0 value within the 0.001-0.01m range [5,6,7] estimated for the Viking and Pathfinder landing sites [8,9]. Two different aerodynamic roughness maps on Mars were recently derived using high-resolution laser altimetry using data from the Mars Orbiter Laser Altimeter (MOLA) aboard Mars Global Surveyor (MGS) [10]. Here, we demonstrate the possibility of using rock abundance maps [11,12] to estimate the roughness density λ as well as some other rock-size frequency parameters (mean diameter D, mean height H) on Mars, and to retrieve subsequently the aerodynamic roughness z_0 by using a quantitative relationships based on wind-tunnel and field measurements on Earth (Fig. 1). Our calculations have been further validated using rock-size frequency distributions inferred from different Martian landing sites and Earth analogs [14,15].

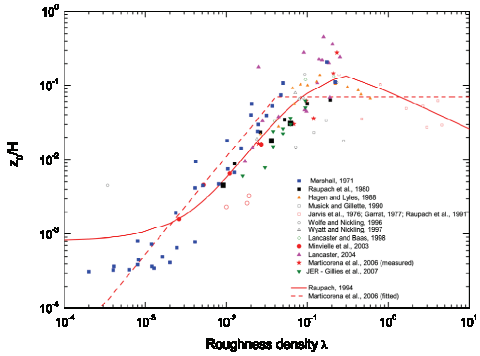

Figure 1: Ratio of the aerodynamic roughness length z_0 to the mean roughness elements height H as a function of the roughness density λ [13].

Previous works on this topic have been mainly dedicated to better assess the quality of the landing sites [16,17,18,19]. As a consequence, the attention has been mainly focused on the bigger rocks distribution, a critical point for characterizing a landing site, that is well reproduced by their chosen exponential fits to the observational data. However, surface roughness can be principally driven by the smallest rocks, and log-normal distributions seem to be better adapted to reproduce with a comparable quality the various-sized components (Fig. 2).

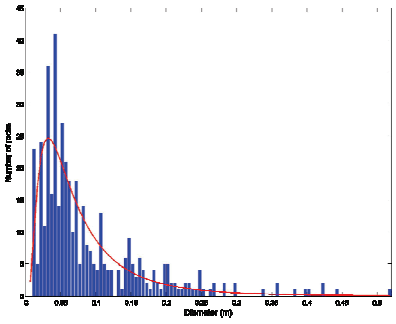

Figure 2.a: Histograms reporting the number of rocks for each size bin diameter at Viking lander 1, along with our fitted log-normal distributions (in red).

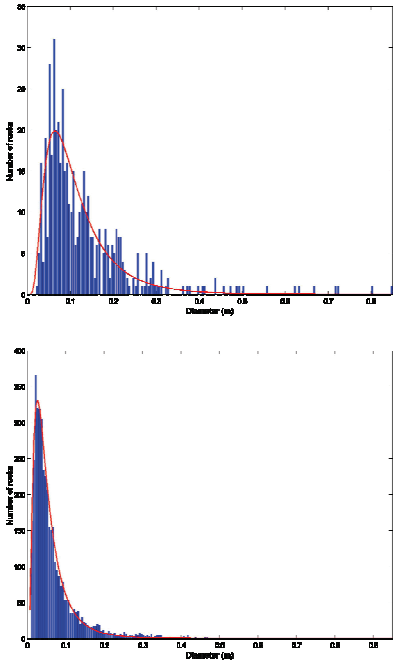

Figure 2.b: Same as figure 2.a for Viking lander 2 and Mars Pathfinder landing sites.

In the next section we build an extended rock abundance map between 87°N and 87°S and deduce the extended roughness map from it. We use the established equations linking D, H, the rock abundance and the roughness density λ to derive the roughness length z_0 using [13].

Extrapolation to high latitudes:

Extending the range of our calculations poleward, well beyond the current limited coverage between latitudes 60°S and 60°N, is a mandatory task before using such maps in MGCM. To do so, we built upon the correlation existing between the albedo, the thermal inertia, and the rock abundance MGS-TES datasets [12,20,21].

The [60°S:60°N] region of Mars.

On the [60°S:60°N] martian map ((1/8)° x (1/8)° resolution), the albedo values range between 0.06 and 0.32. The inertia values are within the range 0-5000 tiu (thermal inertia units) with the majority of the points below 1000 tiu. We constructed 2D-bins of inertia and albedo $[I_k,\alpha_l] = [I_k +/- \Delta I/2, \alpha_l +/- \Delta\alpha/2]$ with $\Delta I = 8$ and $\Delta\alpha = 0.006$. Figure 3 is a map depicting the density of grid points on the albedo and inertia maps whose values belong to a certain 2D-bin. In other words, the plot shows for each $[I_k,\alpha_l]$ bin, the number of (1/8)°x(1/8)° pixels of the I_k and α_l maps having simultaneously an inertia value between $I_k - \Delta I/2$ and $I_k + \Delta I/2$, and an albedo value between $\alpha_l - \Delta\alpha/2$ and $\alpha_l + \Delta\alpha/2$.

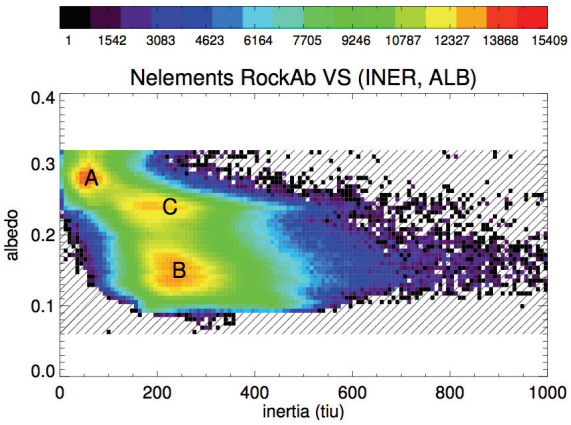

Figure 3: Density of points throughout the different $[I_k,\alpha_l]$ bins. The A, B, and C units are indicated, as defined by [22]. The grey area correspond to empty bins. For convenience we limite the map to inertia values < 1000 tiu.

This map clearly displays three modes for the density, (low I-high α), (high I-low α) and (moderate to high I-intermediate α), as pointed out already by [22] who defined the corresponding A, B an C soil type, respectively.

In each $[I_k,\alpha_l]$ bin the points have a corresponding rock abundance distribution (hereafter : bin-distribution) extracted from the corresponding pixels of the rock abundance map. It might be a single point (if there is only one pixel in the bin) or a well defined distribution (fig. 4).

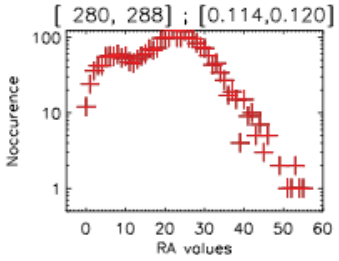

Figure 4: A rock abundance bin-distribution for $[I_k,\alpha_l]$ with I_k=284 and α_l=0.117.

Each non-empty $[I_k,\alpha_l]$ bin has a bin-distribution from which we take the mean and the most probable value (i.e the value with the largest occurrence in the bin). Doing so, we plot two maps similar to the one Fig. 3 except that the color scales are this time correlated to either the mean (Fig. 5) or the most probable (Fig. 6) value of each bin-distribution.

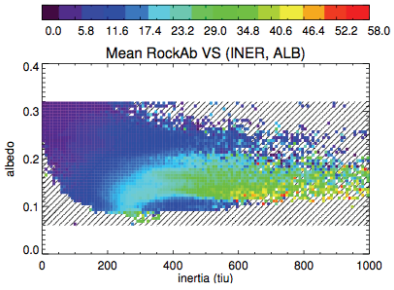

Figure 5: Mean values of the rock abundance bin-distributions. The shape of this density map is the same as the one fig.3, the values in each bin are different.

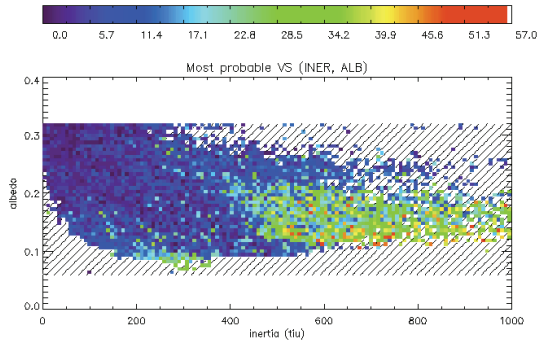

Figure 6: Most probable values of the rock abundance bin-distributions

We now use these maps to fill the rock abundance map poleward of 60°S and 60°N. Inertia and albedo data are available until 87°S and 87°N so that we aim to obtain a rock-abundance map filled between these high latitudes (and so a roughness map as well).

The north band [50°N:60°N] and the south band [60°S:50°S]

Before doing the extrapolation of the rock abundance values, one might want to use the closest region to the poles as a reference in order to avoid biases caused by terrain too far from the regions to fill. It allows as well to get rid of bi-modal bin-distributions such as the one showed on fig.4. On an 'areographical' and geological basis, it is more relevant to consider both north and south bands ([50°N:60°N] and [60°S:50°S] respectively) for an extrapolation of rock abundance values to the north pole and the south pole, respectively. We show fig.7 and fig.8 the density of points throughout the different bins.

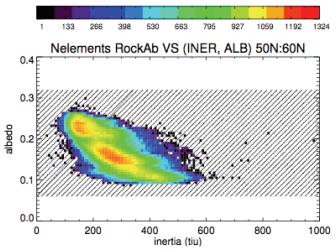

Figure 7: Density of points throughout the $[I_k,\alpha_l]$ bins in the north band [50°N:60°N].

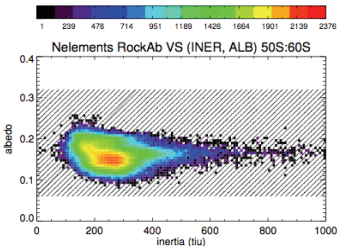

Figure 8: Density of points throughout the $[I_k,\alpha_l]$ bins in the south band [60°S:50°S].

The A unit (see fig. 3) is now missing and B and C units are somewhat modifed (this variations justify the need of considering these bands before extrapolating the rock abundance values).

However the $[I_k,\alpha_l]$ bin coverage of both north band and south band is weaker than the one in the poles (especially in the north pole) and one needs to consider the entire [60°S:60°N] region (central region) as well. Furthermore, the $[I_k,\alpha_l]$ bin coverage is greater in the north pole than the one in the central region (fig.8) as well. Thus some pixels remained unfilled, corresponding to the exposed ice at the surface of the polar regions.

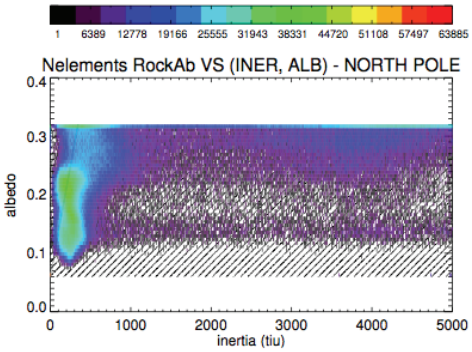

Figure 9: The density of points throughout the $[I_k,\alpha_l]$ bins in the north pole. Much more inertia values greater than 1000 tiu are involved in the different bins than in the central region (see fig. 3).

The extended roughness map

In order to estimate the rock abundance values at the poles we proceed as following. Considering for instance the south pole, for each non-empty $[I_k,\alpha_l]$ bin present in the south pole we check for the corresponding rock abundance value in the reference density maps (in either the south band or the central region if the information is missing from the south band). As a reference rock abundance value we have chosen the most probable one (and not the mean value) because it provided the lowest discontinuities at the borders (60°S and 60°N). The rock abundance map we obtained is shown fig.10.

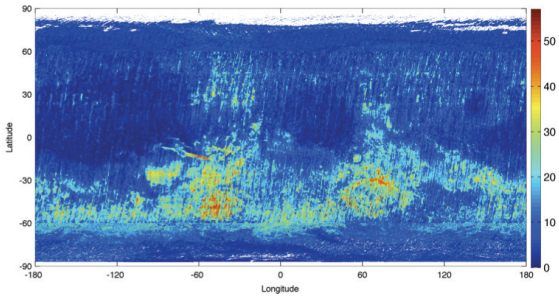

Figure 10: The extended rock abundance map between 87°N and 87°S. Unfilled pixels remain at the Poles (white areas on the map), due to high thermal inertia values of exposed ice sheets. These values are not found in the central region used as a reference, thus preventing from any extrapolation of the rock abundance in these restrained polar regions.

Using the equations derived from the study explain in the second section of this abstract we were able to derive an extended roughness map, between latitudes 87°N and 87°S. The roughness map we obtained is shown fig. 11.

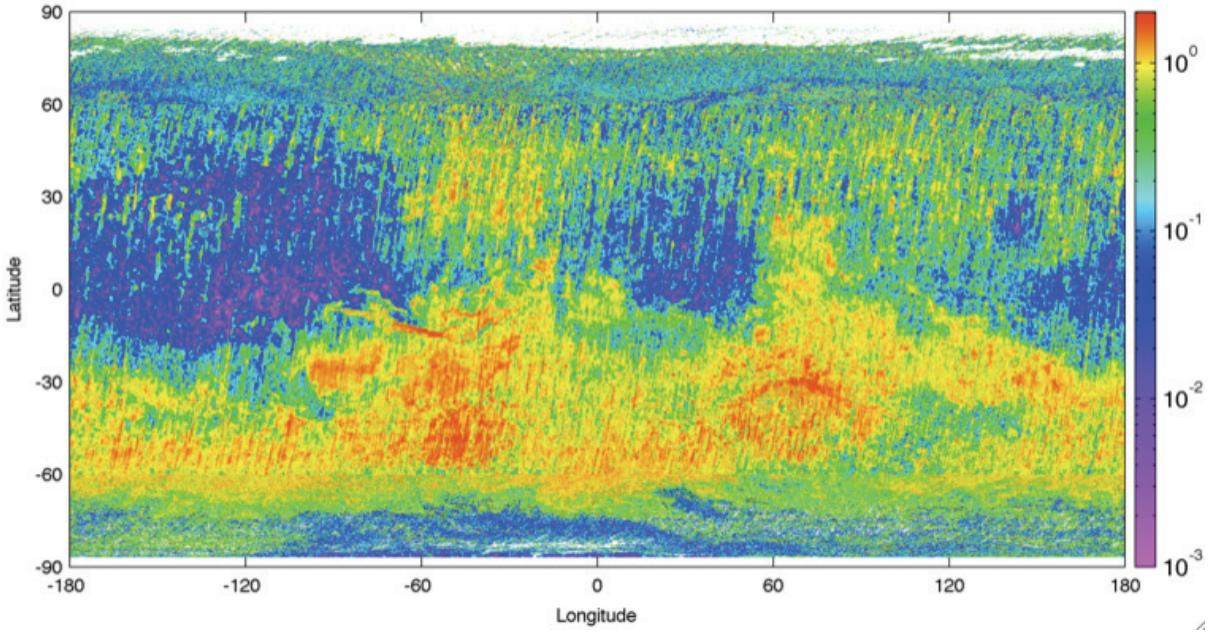

Figure 11: The extended roughness map covering the 87°N - 87°S latitude range. The roughness length is ranging from 0.001 cm (purple) to ~2 cm (red). As in figure 10, white areas correspond to pixels left unfilled (region with exposed ice at the surface and high thermal inertia values).

Conclusion :

We have been able to generate a consistent aerodynamic roughness length z_0 map on the whole surface of Mars. Compared to what has been inferred previously from different landing sites, our results suggest that the method used here to estimate the aerodynamic roughness length z_0 provides a reasonable picture of the actual conditions existing on Mars.

References:

[1] B.A. Cantor (2007). *Icarus, 186*, 60-96.

[2] C.E. Newman, S.R. Lewis, P.L. Read, and F. Forget. (2002). *J. Geophys. Res. - Planet., 107*, E125124.

[3] S. Basu, J. Wilson, M. Richardson, and A. Ingersoll (2006). *J. Geophys. Res. - Planet., 111*, E09004.

[4] M. A. Kahre, J. R. Murphy and R. M. Haberle (2006). *J. Geophys. Res., 111*, E06008.

[5] L. Montabone, S.R. Lewis, and P.L. Read (2005). *Adv. Space Res., 36*, 2146-2155,.

[6] M.A. Kahre, J.R. Murphy, and R.M. Haberle (2006). *J. Geophys. Res. - Planet., 111*, E06008.

[7] C.E. Newman, S.R. Lewis, P.L. Read, and F. Forget (2002). *J. Geophys. Res. - Planet., 107*, E125123.

[8] J.L. Sutton, C.B. Leovy, and J.E. Tillman (1978). *J. Atmos. Sci., 35*, 2346-2355.

[9] R. Sullivan, R. Greeley, M. Kraft, G. Wilson, M. Golombek, K. Herkenhoff, J. Murphy, and P. Smith (2000). *J. Geophys. Res. - Planet., 105*, 24547-24562.

[10] N.G. Heavens, M.I. Richardson and A.D. Toigo. (2008) *J. Geophys. Res., 113*, E02014.

[11] P.R. Christensen. (1986) *Icarus, 68*, 217-238.

[12] S.A. Nowicki and P.R. Christensen (2007). *J. Geophys. Res. - Planet., 112*, E05007.

[13] B. Marticorena, M. Kardous, G. Bergametti, Y. Callot, P. Chazette, H. Khatteli, S. Le Hégarat-Mascle, M. Maillé, J.-L. Rajot, D. Vidal-Madjar and M. Zribi (2006). *J. Geophys. Res. - Earth, 111*, F03017.

[14] N. Lancaster (2004). *Earth Surf. Process. Landforms*, 29, 853-867.

[15] R.A. Yingst, A.F.C. Haldemann, K.L. Biedermann, and A.M. Monhea. (2007). *J. Geophys. Res. - Planet., 112*, E06002.

[16] M. Golombek and D. Rapp (1997). *J. Geophys. Res. - Planet., 10*2, 4117-4129.

[17] M.P. Golombek, A.F.C. Haldemann, N.K. Forsberg-Taylor, E.N. DiMaggio, R.D. Schroeder, B.M. Jakosky, M.T. Mellon, and J.R. Matijevic (2003). *J. Geophys. Res. - Planet., 108*, E128086.

[18] M.P. Golombek, R.E. Arvidson, J.F. Bell, P.R. Christensen, J.A. Crisp, L.S. Crumpler, B.L. Ehlmann, R.L. Fergason, J.A. Grant, R. Greeley, A.F.C. Haldemann, D.M. Kass, T.J. Parker, J.T. Schofield, S.W. Squyres, and R.W. Zurek (2005). *Nature, 436*, 44-48.

[19] M.P. Golombek, A. Huertas, J. Marlow, B. mcGrane, C. Klein, M. Martinez, R.E.Arvidson, T. Heet, L. Barry, K. Seelos, D. Adams, W. Li, J. R. Matijevic, T. Parker, H.G. Sizemore, M. Mellon, A.S. McEwen, L.K. Tamppari (2008). *J. Geophys. Res. - Planet., 113*, E00A09.

[20] P.R. Christensen et al. (2001). *J. Geophys. Res. - Planet., 106*, 23823-23871.

[21] N.E. Putzig, M.T. Mellon, (2007). *Icarus*, 191, 68–94.

[22] M. T. Mellon, B. M. Jakosky, H. H. Kieffer, P. R., Christensen (2000). *Icarus*, 148, 2, 437-455.